

ORIGINAL ARTICLE

Open Access



Research on the Encapsulation Device for Lunar Samples

Yonggang Du^{1*} , Chunyong Wang¹, Haoling Li¹, Ying Zhou¹, Ming Ji¹ and Xuesong Wang¹

Abstract

The encapsulation of lunar samples is a core research area in the third phase of the Chinese Lunar Exploration Program. The seal assembly, opening and closing mechanism (OCM), and locking mechanism are the core components of the encapsulation device of the lunar samples, and the requirements of a tight seal, lightweight, and low power make the design of these core components difficult. In this study, a combined sealing assembly, OCM, and locking mechanism were investigated for the device. The sealing architecture consists of rubber and an Ag-In alloy, and a theory was built to analyze the seal. Experiments of the electroplate Au coating on the knife-edge revealed that the hermetic seal can be significantly improved. The driving principle for coaxial double-helical pairs was investigated and used to design the OCM. Moreover, a locking mechanism was created using an electric initiating explosive device with orifice damping. By optimizing the design, the output parameters were adjusted to meet the requirements of the lunar explorer. The experimental results showed that the helium leak rate of the test pieces were not more than $5 \times 10^{-11} \text{ Pa}\cdot\text{m}^3\cdot\text{s}^{-1}$, the minimum power of the OCM was 0.3 W, and the total weight of the principle prototype was 2.9 kg. The explosive driven locking mechanism has low impact. This investigation solved the difficulties in achieving tight seal, light weight, and low power for the lunar explorer, and the results can also be used to explore other extraterrestrial objects in the future.

Keywords Lunar samples, Encapsulation, Vacuum seal, Mechanism

1 Introduction

The study of lunar samples helps humans investigate the origin and evolutionary history of the moon, and it also contributes to understanding the evolution of the solar system; thus, it has profound scientific significance [1, 2]. To achieve the research goal of lunar samples, the lunar sample and return mission (SRM) must be first completed, and the encapsulation of the lunar samples is one of the core tasks.

The moon is the nearest celestial body to the earth and is the primary goal of deep-space exploration programs. The United States and the former Soviet Union were the

first countries to investigate the encapsulation of lunar samples. The encapsulation device for lunar samples developed by the former Soviet Union used the sealing assembly of a rubber-ring. Its opening and closing mechanism (OCM) is a hinge mechanism driven by an explosive device, and its locking unit is a simple-barbed structure [3]. The United States obtained lunar samples through the Apollo Project, in which the encapsulation device was a box. The box used a sealing assembly of metal and rubber-rings, and the astronaut closed and locked the cover [4].

In a recent development, the explorers that finished the SRM were the Hayabusa explorer of Japan, the Osiris explorer of the United States, and the Chang'e-5 explorer of China. The sample container of Hayabusa-1 adopted two rubber-rings to seal its cover and closed using a linear mechanism driven by a motor, and its locking mechanism was a spring clasp [5].

*Correspondence:

Yonggang Du
dyg@mail@126.com

¹ Lanzhou Institute of Physics, CAST, Lanzhou 730000, China

Subsequently, the Japan Aerospace Exploration Agency (JAXA) studied a seal made of pure aluminum metal, which was then used for the Hayabusa-2 explorer [6]. The Osiris explorer may have used fluorine-rings to seal asteroid samples [7]. Because the Osiris detector will return to Earth by 2023, its sealing performance is unknown. Since 2010, China has started research on encapsulation of lunar samples, and the research results were used for the Chang'e-5 explorer, which completed the lunar SRM in December 2020 [8]. The encapsulation subsystem of the Chang'e-5 explorer was a self-contained system. Its integrated mechanical unit could independently complete the functions of unlocking, opening, closing, and locking for the cover. Its hermetic sealing unit used a combined sealing assembly with a rubber-ring and a metal knife-edge [9].

Researchers are currently studying and developing encapsulation device for samples of extra-terrestrial objects. Since 2009, the United States has studied many sealing architectures for Mars SRMs [10–13], including rubber-rings, soft metals [14, 15], knife-edges [16], metal welding [17], explosive joining [18], and the ongoing shape memory alloy (SMA) [19, 20]. Both rubber-rings and soft metal seals are manufactured by extruding structures (such as knife edges) in rubber or soft metal. Rubber-rings can be sealed at a leak rate of 10^{-4} – 10^{-8} Pa·m³·s⁻¹. Soft metals can be sealed at a leak rate of 10^{-8} – 10^{-11} Pa·m³·s⁻¹. Thus far, the only research results applied to sample sealing for extraterrestrial objects are for rubber and soft metal seals. A metal welding seal is used to weld the low-melting metal in the groove of the cover. The metal is then melted by heating and cooled to form a seal. The explosive joining process uses an explosively driven, high-velocity, angular collision of the metal to weld the contact surfaces and seal the cover. The leak rates of the metal welding and explosive joining are better than 10^{-11} Pa·m³·s⁻¹. The SMA seal is a new concept for the Mars Sample Return 2020 (MSR 2020) program developed by the United States. The SMA seal uses the SMA shape memory effect to create a hermetic seal. The National Aeronautics and Space Administration (NASA) reported that the leak rate of the SMA seal was better than 2×10^{-11} Pa·m³·s⁻¹. America has also studied containers for Martian atmospheric samples [21]. This container was sealed with Teflon, and a valve was used to open and close the sampling hole.

Based on the application of the Chinese Lunar Exploration Program, the researchers investigated an encapsulation device and confirmed the results through simulation and tests.

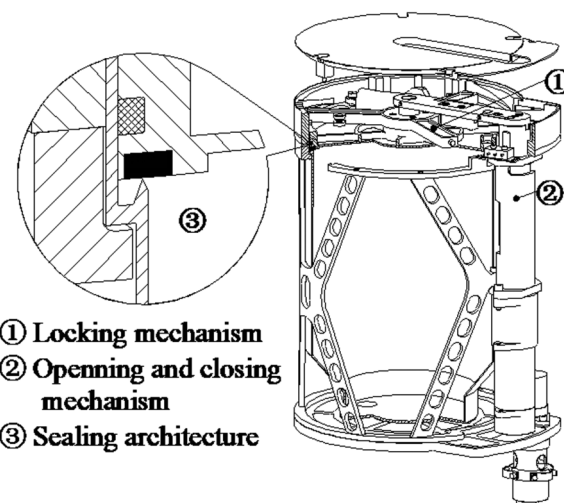


Figure 1 Composition of the encapsulation device

2 System Description

The encapsulation device for lunar samples is used to seal lunar samples. The hermetic sealing unit and mechanical unit are the cores of the encapsulation device. Figure 1 shows the makeup of the encapsulation device.

Hermetic sealing is a key technology for sealing lunar samples and for preventing contamination. The sealing unit uses a combined sealing architecture of rubber and Ag-In alloy. This sealing architecture takes advantage of a rubber ring and a metal seal, and this seal is also easy to fabricate.

The locking mechanism, OCM, and structure comprise a mechanical unit. Because the structural part is well known, it is not described in this study. The opening mechanism functions by moving the cover away from the sealing architecture in a straight line and then rotating it open, and the closing process is the opposite. Therefore, we have studied a new combined mechanism driven by a single motor that uses a coaxial double helical pair to move the cover in a linear motion or rotational motion. The locking mechanism is a rocker arm driven by an explosive actuator, the key technology for which is orifice damping. It locks the lid by applying a sealing force. These technologies make the device smaller and lighter.

The sealing and mechanism units are closely connected. The sealing architecture determines the design of the OCM and locking mechanism. The process for the study is to first find the linear displacement and minimum sealing force of the sealing unit and then design the transmission of the mechanism unit based on these parameters.

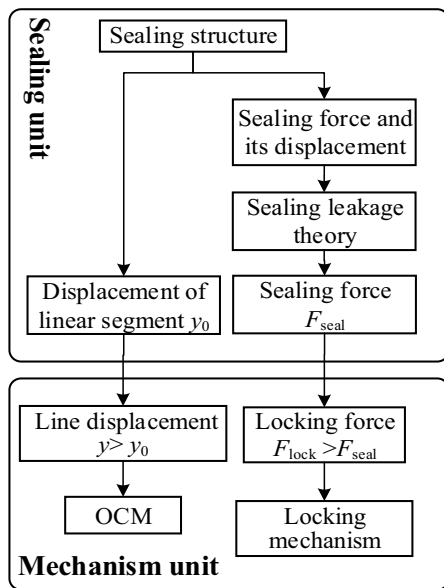


Figure 2 Process of the research

The linear displacement of the OCM must be greater than the thickness of the lid because the cover can enter or separate from the sealing architecture in a straight line. The locking mechanism applies a sealing force to the sealing structure, and its value must be greater than the minimum value required. Figure 2 shows the research process, including the association between the sealing unit and mechanism.

3 Sealing Unit

3.1 Sealing Architecture

The outer and inner seals of the sealing architecture are rubber-ring and edge seals, respectively, as shown in Figure 3. A rubber-ring is a low-temperature fluorine-rubber that can handle a low-temperature environment on the lunar surface. The material used for metal sealing was an Ag-In alloy, and the knife-edge was a titanium alloy. Indium is frequently used as a hermetic sealing material because of its excellent mechanical properties and vacuum stability [22]. In this study, the melting point of the Ag-In alloy was 170–176 °C. This alloy adapts well to the environment of lunar surface. The hardness of the Ag-In alloy is approximately Shore 50; thus, the force of knife-edge pressing in the Ag-In alloy is reasonable.

Figure 3 shows that the cover of the lunar sample container can only enter or separate from the sealing architecture in a linear motion along the axis of the container. The cover is first lifted by the OCM and rotated counter-clockwise for opening, rotated clockwise, and then falls into the sealing architecture for closing. Finally, the locking

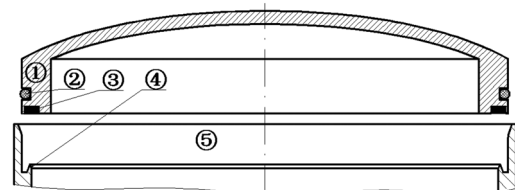


Figure 3 Composition of the sealing unit

mechanism applies a sealing force on the knife-edge and locks the lid.

According to the design of the sealing unit, the output displacement of the linear motion of the OCM was 41 ± 1 mm and the output angle was $120^\circ \pm 1^\circ$. Through simulation, we obtained information about the sealing force and linear movement of the sealing unit. These parameters were used to design the mechanism unit.

3.2 Sealing Force and Linear Displacement

Previous studies have shown that the depth of the knife-edge pressed into the Ag-In alloy must be larger than the threshold value for effective hermetic sealing. The inside of the rubber-ring should maintain stress to create a seal; therefore, the sealing force determines the sealing performance. During the sealing process, the compression of the rubber-ring, friction, and extrusion of the knife-edge pressing into the Ag-In alloy all work together to create a sealing force. We calculated the law between the sealing force and displacement and used it to determine the minimum sealing force and displacement required to make a hermetic seal.

The sealing force is divided into two parts: The first part is the resultant force of the extrusion force and friction of the rubber-ring, and the other is the force of the knife-edge pressing into the Ag-In alloy. The sealing process creates a hermetic seal with a rubber-ring first, followed by an edge seal. The change in sealing force consists of three stages. The first stage involves squeezing the rubber-ring into the sealing structure. The second stage involves sliding the rubber-ring along the axis of the container, and the third stage involves pressing the knife-edge into the Ag-In alloy.

In this study, the finite element method (FEM) analysis was used to calculate the change law of the sealing force in the three stages. The element of the finite element model was an axial symmetry plane element, and the fillet of the tooltip was R0.1 mm. The Moony-Rivlin model describes the material model of the rubber and agrees well with the experimental data on the rubber material. The Moony-Rivlin material model is based on the following expression:

$$W_d = C_1(I_1 - 3) + C_2(I_2 - 3), \tag{1}$$

Table 1 Parameters of the Moony-Rivlin model

c_1	c_2	f	$\rho_{\text{rubber}} \text{ (g}\cdot\text{cm}^{-3}\text{)}$
1.5862	0.09504	0.25	1.19

Table 2 Parameters of the Ag-In alloy

Elastic	Elastic modulus E_1 (GPa)	1–3
	Poisson's ratio	0.42
Plastic	Yield stress (MPa)	10–29

Table 3 Parameters of the titanium alloy

Item	Elastic modulus E_2 (GPa)	Poisson's ratio	Density ρ_T (g·cm ⁻³)
Value	110	0.3	4.7

where W_d is the strain energy density. C_1 and C_2 are the dimensionless material constants fitted to the test data. I_1 and I_2 are the principal invariants of the Cauchy-Green deformation tensor. The model also has friction between the rubber ring and metal, and the friction coefficient is f . Table 1 lists the parameters of the rubber material.

We used an elastic-plastic model to describe the Ag-In alloy. The parameters of the elastic-plastic model presented in Table 2, which obtained by calculating the

test results. The knife-edge material is a titanium alloy, described as an elastic material model. The parameters of the titanium alloy are listed in Table 3.

The three layers shown in Figure 4 are responsible for the sealing force and displacement. The top layer indicates the state of each stage. The second layer is the relationship between each sealing force and the sealing displacement, and the third layer indicates the association between the sealing force and the displacement over the entire process.

The motion of the sealing process is in a straight line, over a displacement of 4.7 mm, and requires a minimum force of 3890 N. The first stage had a displacement of 2.1 mm and strength of 118 N. The second stage had a friction of 107 N and displacement of 2 mm. In the third stage, the sealing force was 3890 N, and the distance was approximately 0.6 mm.

3.3 Theory of Sealing Leak Rate

Figure 3 shows that the sealing assembly is a tandem mechanical seal made of a rubber-ring and an Ag-In alloy. The theory of sealing leak rate is built based on the micro porous-molecular flow theory.

According to Roth's theory, the leak rate depends on the contact parameters of the sealing surface, such as average stress, contact width, and contact length. In this study, the contact parameters were calculated using FEM analysis.

The contact width of the sealing face of the rubber and its contact stress at different positions along the width are

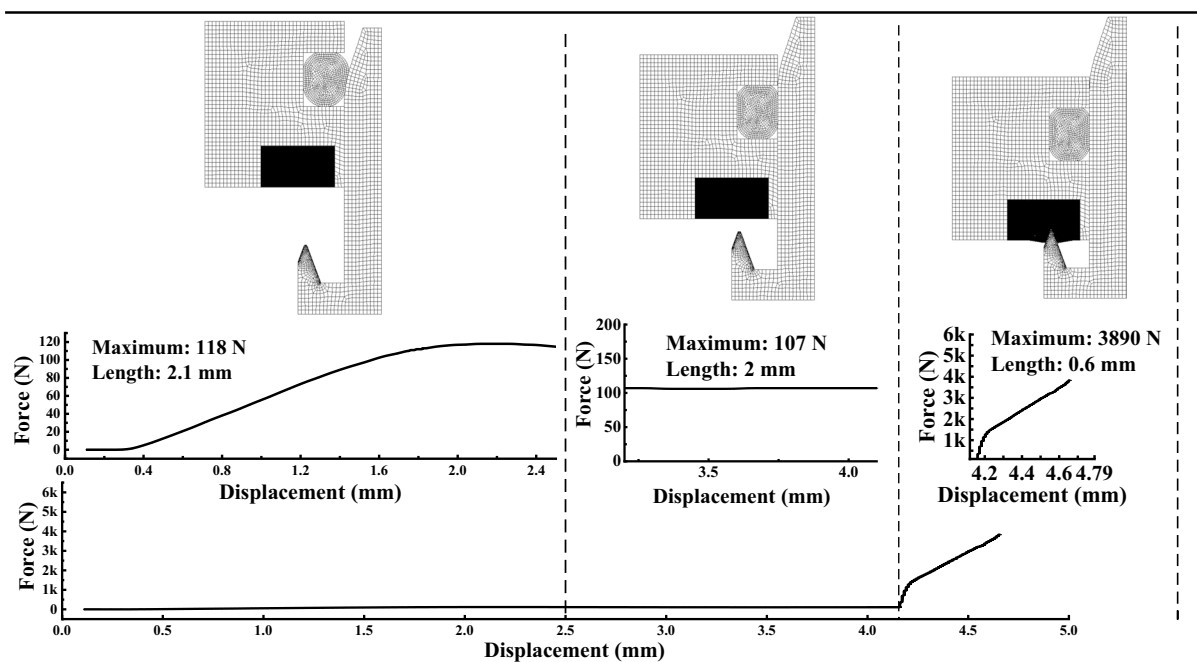


Figure 4 Change law of sealing force in the sealing process

shown in Figure 5(a). The abscissa in Figure 5(a) represents the position of the contact face, and the longitudinal axes represent the contact stresses. Figure 5(b) shows the stress distribution in the rubber-ring.

The contact width of the knife-edge and stress at different contact positions are displayed in Figure 6(a). The abscissa in Figure 6(a) is the X-axis of the contact cross-section, and the left longitudinal axis is the Y-axis of the contact cross-section (the cross-section is in the XY plane). The right longitudinal axis represents the contact stress of the Ag-In alloy. Figure 6(b) shows the stress distribution in the Ag-In alloy.

Based on the hypothesis of molecular flow, Chang et al. [23] proposed a theory of the hermetic leak rate of a rubber-ring, expressed as Eq. (2):

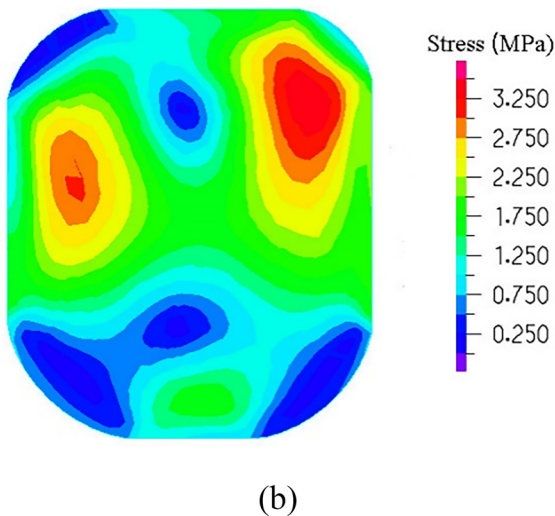
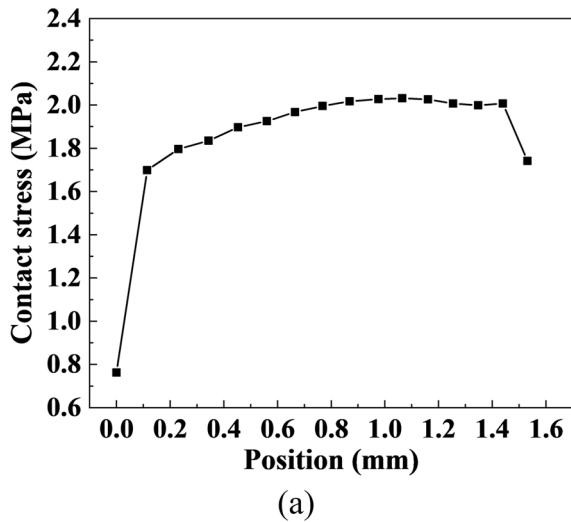


Figure 5 Calculated results of the rubber-ring: (a) Contact positions and contact stress of the rubber-ring, (b) Stress distribution of the rubber-ring

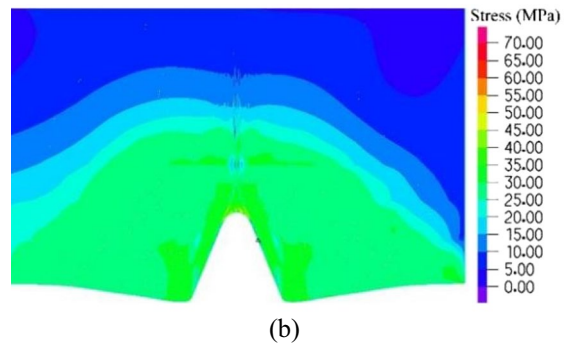
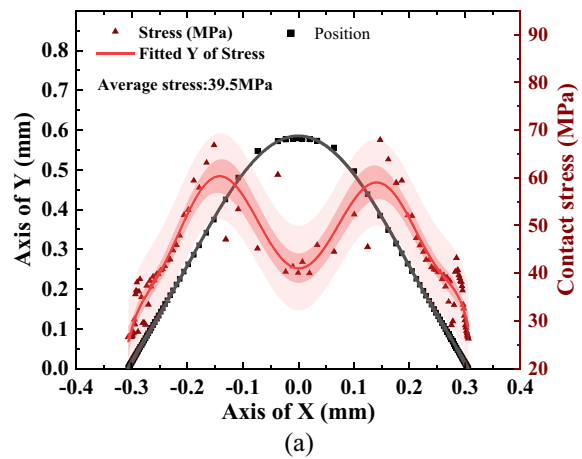


Figure 6 Calculated results of the Ag-In alloy: (a) Contact positions and contact stress of the Ag-In alloy, (b) Contact stress distribution of the Ag-In alloy

$$Q_1 = 8\sqrt{\frac{T}{M}}H^2\frac{\pi D}{w}\exp\left(\frac{-3\bar{\sigma}}{K_s}\right)\Delta P, \quad (2)$$

where Q_1 is the hermetic leak rate of the rubber-ring, T is the temperature of air in Kelvin, and M is the molar mass of air. H is the height of the micro-leak, is determined by the roughness of the sealing face. D , W , K_s , and ΔP represent the equivalent diameter, effective width, and sealing coefficient. The pressure difference on both sides was ΔP . The average contact stress on the sealing face is $\bar{\sigma}$.

The metal seal of the encapsulation device is an edge seal, which is a metal-metal seal. According to Roth's theory, the hermetic micro-leak rate of a seal is given by the following equation [24, 25]:

$$Q_s = \frac{2}{3}\sqrt{\frac{8RT}{\pi M}}\frac{Kh^3}{w \tan \theta(1 + \frac{1}{\theta})}\Delta P, \quad (3)$$

where Q_s is the hermetic leak rate of a single micro-leak; R is the air constant; θ is the bottom angle of the cross-section of the leakage; and h is the relative height of the leak, which has the following relationship with H :

$$\frac{h}{H} = \exp\left(-\frac{\bar{\sigma}}{K_s}\right). \tag{4}$$

Assuming that the micro-leaks distributed on the sealing face are even, the number of micro-leaks (N) can be expressed using Eq. (5):

$$N = \frac{\pi D \tan \theta}{2H}. \tag{5}$$

The expression for the leak rate of the annular edge seal can be obtained using Eqs. (3)–(5), as shown in Eq. (6):

$$Q_2 = NQ_s = 1.42 \sqrt{\frac{RT}{M}} \frac{DH^2}{w} \exp\left(-\frac{3\bar{\sigma}}{K_s}\right) \Delta P, \tag{6}$$

where Q_2 is the hermetic leak rate of the metal seal. During the machining of a sealing face, the cutting tool leaves many circular marks on the surface, as shown in Figure 7.

The width of the sealing face is defined as $W = \delta_c w$ because there are many circular marks on the face, where δ_c is the contact coefficient with a value of $0 \leq \delta_c \leq 1$. The modified equation shows how well the knife-edge sticks to the Ag-In alloy. When the knife-edge does not stick to the Ag-In alloy, the contact coefficient is $\delta_c = 0$. A contact coefficient of $\delta_c = 1$ indicates that the knife-edge and

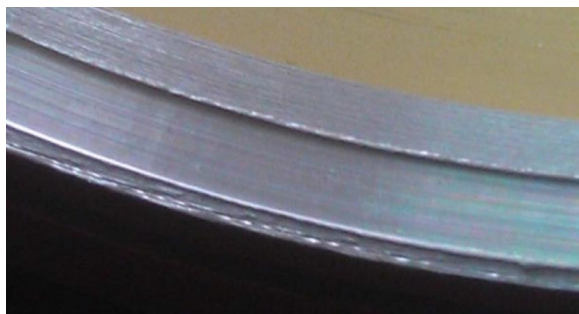


Figure 7 Machining-tool traces on the sealing face

alloy stick together completely. The equation for the hermetic leak rate is as follows:

$$Q_2 = 1.42 \sqrt{\frac{RT}{M}} \frac{DH^2}{\delta_c w} \exp\left(-\frac{3\bar{\sigma}}{K_s}\right) \Delta P. \tag{7}$$

Because the rubber-ring and knife-edge are tandem seals, the equation of the total hermetic leak rate (Q) is given by:

$$Q = \frac{Q_1 Q_2}{Q_2 + Q_1}. \tag{8}$$

The parameters in Table 4 were employed to calculate the seal of the encapsulation device and provide the results in Figure 8. In the figure, the abscissa axis represents the contact coefficient, the ordinate axis represents the hermetic leak rate. Figure 8 indicates that the contact coefficient significantly affected the leak rate.

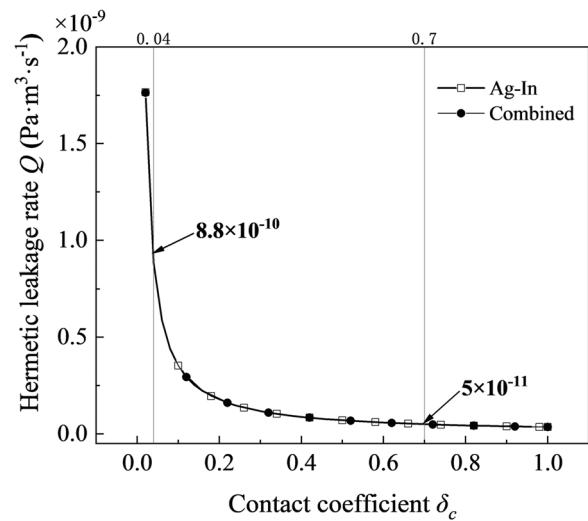


Figure 8 Calculated results of leak rate

Table 4 Parameters of sealing model

Item	Temperature T (K)	Air constant R (J(kg·K) ⁻¹)	Molar mass of air M (kg·mol ⁻¹)	Contact coefficient δ_c	Sealing coefficient K_s (Pa)
Rubber	293.2	287	0.029	0–1	9.9×10^5
Ag-In	293.2	287	0.029	0–1	7.6×10^6
Item	Sealing width W (m)	Height of the micro-leak H (m)	Equivalent diameter D (m)	Pressure difference ΔP (Pa)	Contact stress $\bar{\sigma}$ (Pa)
Rubber	1.5×10^{-3}	8×10^{-7} m	1.65×10^{-1}	1×10^5	1.7×10^6
Ag-In	8.9×10^{-4}	8×10^{-7} m	1.2×10^{-1}	1×10^5	3.95×10^7

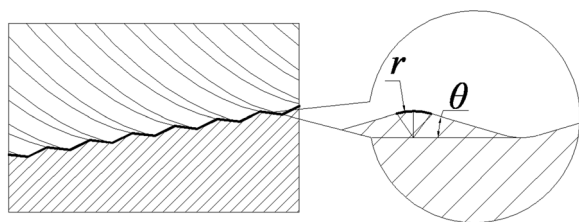


Figure 9 Cutting traces on the sealing face

Table 5 Test results of hermetic leak rate

Sealing force (N)	2940	3430	3920	4410	4900
Depth (mm)	0.45	0.55	0.67	0.76	0.85
Helium leak rate (Pa·m ³ ·s ⁻¹)	≲ 5 × 10 ⁻¹¹				

The slope angle of micro-channels on more than 90% of rough-metal surfaces is 1°–4°, according to a study by Roth [26, 27]. Roth’s theory assumes that the cross-section of the micro-leaks is an isosceles triangle with a base angle of 4°. As shown in Figure 9, the cutting traces on the sealing face are similar to the traces with the cross-section of an isosceles triangle.

The peak fillets of the cutting traces experience the most contact under contact pressure. θ is the slope angle of the micro-channels, which equals 4°, and r is the fillet radius of the peak point of the traces. From Figure 9, it can be seen that the expression for the limiting value of δ_{lim} is given by Eq. (9), where R_a is the roughness value, δ_p is correction factor related to contact pressure. It is estimated that the δ_{lim} equals to 0.04. According to Figure 8 and the value of δ_{lim} , the theoretical minimum value of the hermetic leak rate is $8.8 \times 10^{-10} \text{ Pa}\cdot\text{m}^3\cdot\text{s}^{-1}$ when the sealing surface is not treated. When the hermetic leak rate reaches $5 \times 10^{-11} \text{ Pa}\cdot\text{m}^3\cdot\text{s}^{-1}$, the contact coefficient (δ_c) must be greater than 0.7.

$$\delta_{lim} \approx \frac{r\theta^2}{R_a} \delta_p. \tag{9}$$

These tests proved the validity of the theory. Without Au coating, the test values of the hermetic leak rate were greater than $10^{-9} \text{ Pa}\cdot\text{m}^3\cdot\text{s}^{-1}$. Based on the above analysis, increasing the contact coefficient of the sealing face can decrease the leak rate. Therefore, we proposed electroplating the sealing face with Au as a solution. The principle is that the contact coefficient of the sealing face is increased by filling the cutting traces with the Au coating. Table 5 shows that the helium leak rate of the test pieces can be as low as $5 \times 10^{-11} \text{ Pa}\cdot\text{m}^3\cdot\text{s}^{-1}$ when there is an Au coating on the surface of the knife-edge for cutting



Figure 10 Test pieces with Au coating on the sealing face

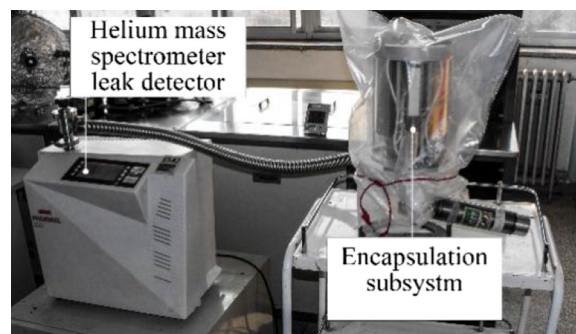


Figure 11 Tests using a helium leak detector

depths greater than 0.45 mm. The test pieces with the Au coating is shown in Figure 10. The test results used the explosive actuator is far greater than the helium leak rates of the test pieces, as shown in Figure 11. The result is due to the piece has finished the vibration test in advance and some other reasons, which will be studied deeply in the research of engineering prototype.

4 Mechanical Unit

4.1 Architecture

The mechanical units of the encapsulation device are the OCM, locking mechanism, and structure. Because the OCM and locking mechanisms are the transmission parts of the device, they are the core parts of the study.

The OCM possesses a motor, shell, guide notch, ping, screw rod, jackshaft, and output-shaft, as shown in Figure 12. As a combined mechanism, the OCM can output linear and rotational displacements in the segments.

Figure 13 illustrates the locking mechanism, which consists of an explosive actuator, locking ring, locker, cover, and wedge groove. The power source of the

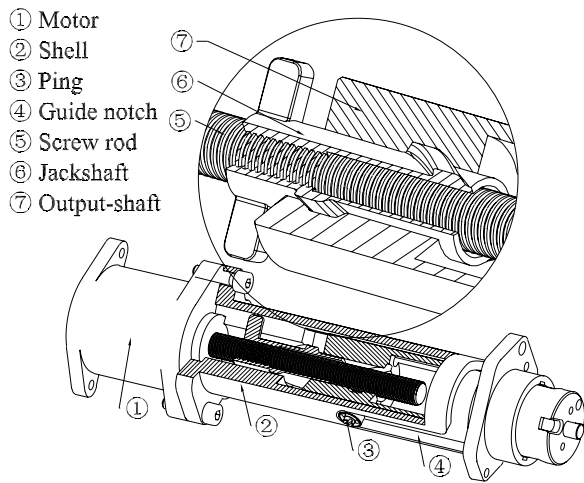


Figure 12 Composition of the OCM

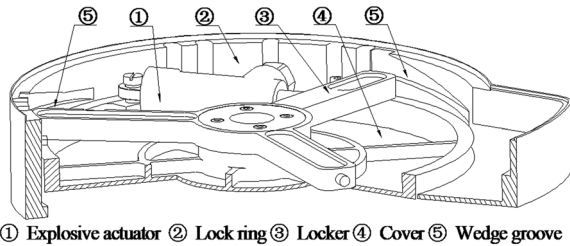


Figure 13 Composition of the locking mechanism

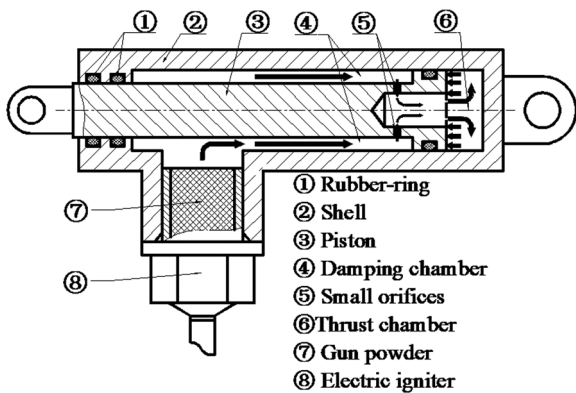


Figure 14 Composition of the explosive actuator

locking mechanism is an explosive actuator, which can apply sufficient force to seal and lock the lid. To prevent the structure from impacting, a damping architecture with small orifices was used to control the speed of the piston by adjusting the gas flowing through the small orifices. The explosive actuator was composed of rubber-rings, a shell, a piston, a damping chamber, a thrust

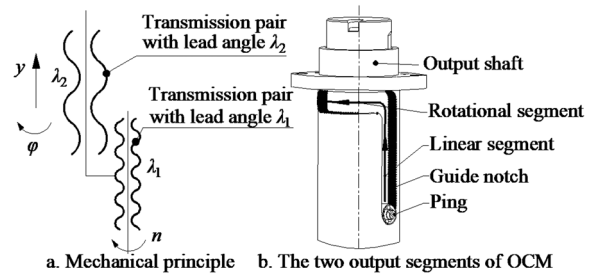


Figure 15 Transmission principle of the OCM

chamber, small orifices, gunpowder, and an electric igniter (Figure 14). The piston divides the interior of the actuator into two parts: the front chamber is the damping chamber (4 in Figure 14) and the rear chamber is the trust chamber (6 in Figure 14).

4.2 Transmission and Verification

4.2.1 Opening and Closing Mechanism

The transmission parts of the OCM are the screw rod, jackshaft, and output-shaft, which are coaxial. The contact surfaces of the transmission parts are coated with a solid molybdenum disulfide (MoS_2) lubricant and thus have a small friction coefficient and high performance in vacuum [28–30]. The OCM has two helical pairs: the screw rod and jackshaft form a helical pair with a lead angle of λ_1 , and the jackshaft and output-shaft form a helical pair with a lead angle of λ_2 . The output-shaft fixes a ping that limits the freedoms of the output-shaft within the guide notch. Because the angle of λ_1 is very small, the revolving screw rod drives the jackshaft and the output-shaft to generate a linear motion when the ping is in the guide notch of the linear segment. The ping limits the linear freedoms of the output-shaft within the guide notch of the rotational segment, and the linear movement of the jackshaft only drives the output shaft to rotate because λ_2 is a large value. The output of the output-shaft is determined by the location of the ping at the guide notch. The transmission principle is illustrated in Figure 15.

The parameters of the OCM were the input, output, and structural parameters. The input parameters were the input torque and speed, and the output parameters were the displacement, velocity, and other parameters output by the OCM. The structural parameters describe the contours of OCM. The matrix of the input torque for the OCM is presented in Eq. (10):

$$T = \Gamma \Psi_1, \tag{10}$$

where T is the matrix of the input torque of the mechanism, defined as $T = \begin{bmatrix} T_L \\ T_R \end{bmatrix}$, which expresses the input

torque parameters. The input torques in the linear and rotational segments are T_L and T_R , respectively. F is the load matrix of the mechanism, defined as $F = \begin{bmatrix} G & 0 \\ G & M_r \end{bmatrix}$, expressing the loads. G is the linear load on the output shaft and M_r is the torque load on the output shaft. Ψ_1 is defined as $\Psi_1 = \begin{bmatrix} \frac{d_2 \tan(\lambda_1 + \rho')}{2} \\ \frac{1 + \mu \tan \lambda_2}{2D_2(\tan \lambda_2 - \mu)} d_2 \tan(\lambda_1 + \rho') \end{bmatrix}$, where d_2 is the pitch diameter of the screw, λ_1 is the lead angle of the screw rod, μ is the friction coefficient, ρ' is the equivalent friction angle, D_2 is the pitch diameter of the jackshaft, and λ_2 is the lead angle of the jackshaft.

The output matrix of the OCM is given by Eq. (11), which represents the displacement, velocity, and other parameters outputted by the OCM.

$$\Xi = \Psi_2 \Theta, \tag{11}$$

where Ξ is the matrix of the output parameters, expressed as $\Xi = [y \ v \ \varphi \ \varphi']^T$; y is the linear displacement; v is the linear velocity; φ is the angle; and φ' is the angular velocity. Ψ_2 is a matrix of structural parameters, defined as $\Psi_2 = [A \ A \ B \ B]^T$, where $A = \frac{d_2 \tan \lambda_1}{2}$ and $B = \frac{d_2 \tan \lambda_1}{D_2 \tan \lambda_2}$. Θ is the matrix of the input parameters of the OCM and $\Theta = [\theta_L \ \omega \ \theta_R \ \omega]$, where θ_L and θ_R are the input angles of the OCM in the linear and rotational segments, respectively, and ω is the input speed of the OCM.

A program was created for the transmission model, and the calculations were performed. A principle prototype was also tested, the results of which are listed in Tables 6 and 7. Figure 16(a) shows the relationship between the input torque (T_R) and output angle (φ). The curves in Figure 16(b) were extended owing to some unmeasurable data, which correctly displayed the trend of the input torque (T_L) with the output displacement (y). The output angle (φ) of the rotational segment was in the range of 0–120.2°, and the input torque was $T_r = 34.3$ –49 mN·m. The output linear displacement was $y = 0$ –41.5 mm, and the input torque was $T_L = 19.6$ –59 mN·m. The data show that the input torque was small.

Table 6 Input parameters of the OCM

Item	Calculation	Experiment
Input torque for linear motion T_L (mN·m)	21.5	19.6–59
Input torque for rotational motion T_R (mN·m)	48.3	34.3–49
Input speed n_r (r/min)	15	–
Input revolution (t)	$\theta_L = 27.5$ $\theta_R = 15.0$	–

Table 7 Output parameters of the OCM

Items	Calculation	Experiment
Linear displacement y (mm)	41.6	41.5
linear speed v (mm·s ⁻¹)	0.38	–
Output angle φ (°)	120	120.2
Time for opening or closing t (s)	169.3	170
Output angular speed φ' (°/s)	2	–

It can be seen from Table 6 that the input speed was 15 r/min, and the input revolution was 43.5 R. Table 7 indicates that the linear and angular displacements were 41.5 mm and 120.2°, and this implies that the lid's opening position will not interfere with the sampler. Table 7 also shows that the output speeds were 0.38

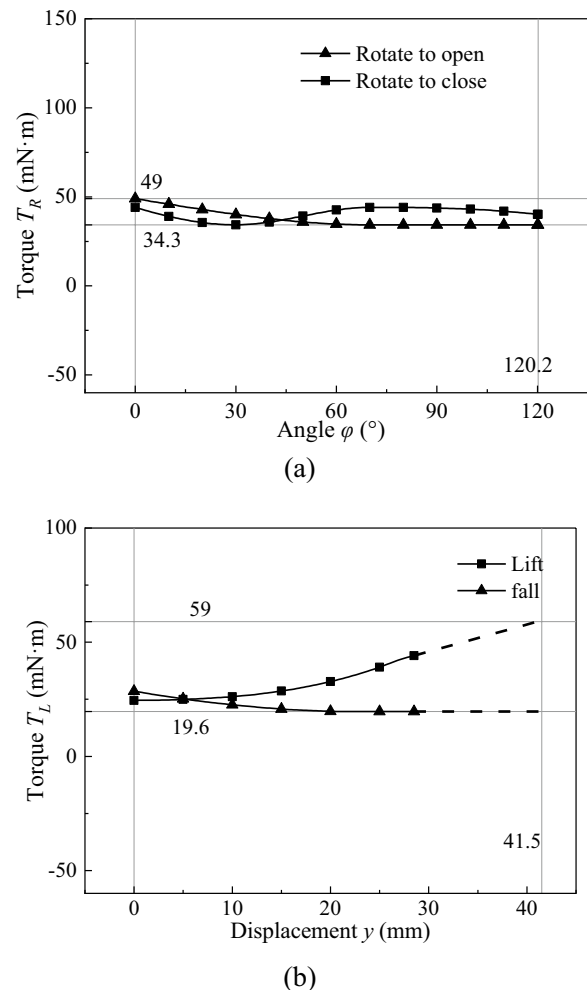


Figure 16 Output parameters of the OCM: (a) Output parameters in rotation, (b) Output parameters for linear motion

Table 8 Parameters of the locking mechanism

Name of parameter	Value
Charge weight ω_p (kg)	2×10^{-3}
Burning rate coefficient of propellant u_0 ($\text{m}\cdot\text{s}^{-1}\cdot\text{Pa}^{-1}$)	5.2×10^{-9}
Thickness of propellant e (m)	8×10^{-3}
Length of propellant c (m)	2×10^{-2}
Burning rate index of propellant n	0.89
Density of propellant ρ ($\text{kg}\cdot\text{m}^{-3}$)	1.6×10^3
Covolume α ($\text{m}^3\cdot\text{kg}^{-1}$)	1×10^{-3}
Power f_p ($\text{J}\cdot\text{kg}^{-1}$)	9.3×10^5
Maximum displacement of the piston x_M (m)	2.1×10^{-2}
Initial volume of the damping chamber V_Z (m^3)	1.5×10^{-6}
Initial volume of the thrust chamber V_d (m^3)	1.2×10^{-7}
Area of the damping hole A (m^2)	1×10^{-6}
Action area of the piston in the damping chamber A_Z (m^2)	3.5×10^{-5}
Action area of the piston in the thrust chamber A_d (m^2)	1.1×10^{-4}
Adiabatic index of gas k	1.3

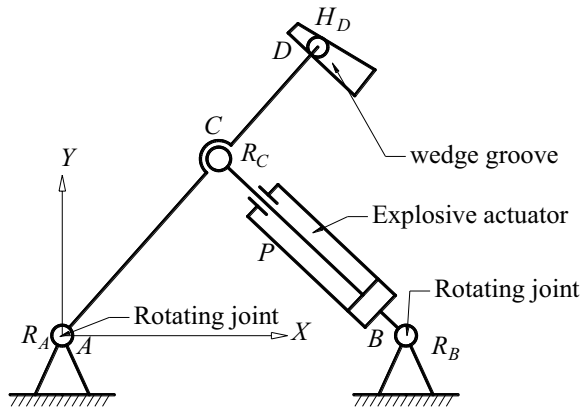


Figure 17 Principle scheme of locking mechanism

$\text{mm}\cdot\text{s}^{-1}$ and $2^\circ/\text{s}$; thus, the opening or closing time was $t = y/v + \varphi/\varphi' = 41.5/0.38 + 120.2/2 = 169.3$ s. The minimum input power was $P = T_{\min}nS/9550\eta = (59 \times 15 \times 2)/(9550 \times 0.6) \approx 0.3$ W, where T_{\min} is the minimum input torque required, n_r is the input speed, S is the safety factor, and η is the efficiency.

4.2.2 Locking Mechanism

The locking mechanism is a rocker arm driven by an explosive actuator. The rotation center of the rocker was a rotating joint, R_A . The explosive actuator can be regarded as a parallel pair, called P , and the two ends of the explosive actuator are the rotating joints (R_B and R_C). The end of the rocker arm is a screw pair, termed H_D , and the parallel pair (P) drives the rocker

arm around A . The screw pair (H_D) moves the locking mechanism along the Z axis (i.e., the direction is perpendicular to the X and Y planes). Figure 17 shows the manner in which the locking mechanism operates.

From the previous discussion, the explosive actuator is both a power source and a damping device; therefore, its dynamic model is essential for understanding the locking mechanism. First, a mechanical model of the explosive actuator was built. Eq. (12) is the propellant combustion equation for the explosive actuator [31].

$$\frac{d\Omega}{dt} = \frac{1}{e} \chi (1 + 2\lambda Z + 3\mu_p Z^2) \frac{de_t}{dt}, \quad (12)$$

where Ω is the percentage of the whole gun propellant burned and Z is the thickness of the gun propellant. λ , μ_p , and χ are the main characteristics of the shape, and e_t is the thickness of the gun propellant burned at time t . The burning rate of the gun propellant is expressed by Eq. (13):

$$\frac{de_t}{dt} = u_0 P_Z^n, \quad (13)$$

where u_0 is the burning rate coefficient and n is the pressure index of the burning rate.

The gas equation of the propellant is the Noble-Abel state equation [32]. After differential operation, the function of the gas pressure in the damping chamber is given by Eq. (14):

$$\frac{dP_Z}{dt} = \frac{\omega_p (f_p \delta_z - P_Z (\frac{1}{\rho} - \alpha)) \frac{d\Omega}{dt} - (f \delta_z + P_Z \alpha) \frac{dG_M}{dt} + P_Z A_Z \frac{dx}{dt}}{V_Z - \frac{\omega_p (1 - \Omega)}{\rho} - (\omega_p \Omega - G_M) \alpha - A_Z x_M}, \quad (14)$$

where P_Z is the pressure in the damping chamber and ω_p is the charge weight. f_p is the power and α is the covolume. ρ is the density and δ_z is the temperature correction factor of the gas in the damping chamber. G_M is the amount of gas flowing from the damping chamber to the thrust chamber. x is the displacement of the piston and x_M is its maximum. V_Z is the initial volume of the damping chamber and A_Z is the action area of the piston in the damping chamber.

The pressure change rate in the trust chamber is expressed by the following equation:

$$\frac{dP_d}{dt} = \frac{(f_p \delta_z \delta_d + P_d \alpha) \frac{dG_M}{dt} - P_d A_d \frac{dx}{dt}}{V_d - G_M \alpha + A_d x_M}, \quad (15)$$

where P_d denotes the pressure in the thrust chamber. δ_d is the temperature correction coefficient of the gas in the thrust chamber. V_d is the initial volume of the thrust

chamber and A_d is the action area of the piston in the thrust chamber.

The gas flows from the damping chamber into the thrust chamber through small orifices, and the equation of the gas mass is given by Eq. (16):

$$\frac{dG_M}{dt} = \begin{cases} AP_Z \sqrt{\frac{2k}{f\delta_z(k-1)} \left(\left(\frac{P_Z}{P_d}\right)^{\frac{-2}{k}} - \left(\frac{P_Z}{P_d}\right)^{\frac{k+1}{k}} \right)}, & \text{when } \frac{P_Z}{P_d} < \left(\frac{k+1}{2}\right)^{\frac{k}{k-1}}, \\ AP_Z \sqrt{\frac{k}{f\delta_z} \left(\frac{2}{k+1}\right)^{\frac{k+1}{k-1}}}, & \text{when } \frac{P_Z}{P_d} \geq \left(\frac{k+1}{2}\right)^{\frac{k}{k-1}}, \end{cases} \quad (16)$$

where A is the area of the small orifices and k is the adiabatic index of the gas. Eq. (17) expresses the dynamic equation of the piston.

$$F + P_d A_d - P_Z A_Z = m \frac{dv_p}{dt}, \quad (17)$$

where F is the load force and m is the mass of the piston. The speed of the piston is $v_p = dx/dt$; thus, the transmission model for the locking mechanism is as follows:

$$\begin{cases} F_L = \frac{L_{AC}}{L_{AD}} F_W \sin \Phi_m \tan(\lambda_I + \rho'), \\ y_L = L_{AD} \Phi_O \tan \lambda_I, \end{cases} \quad (18)$$

where F_L is the output force of the locking mechanism and F_W is the force outputted by the explosive actuator. L_{AC} , L_{AB} , and L_{BC} are the lengths of the kinematic pairs,

as shown in Figure 17. The lead angle of the wedge groove was λ_I . Φ_O is the angle between the AC arm and X -axis, expressed as $\Phi_O = \arccos\left(\frac{L_{AB}^2 + L_{AC}^2 - (L_{BC} + x)^2}{2L_{AC}L_{AB}}\right)$, $0 < \Phi_O \leq \pi/2$. The angle between AC and BC is Φ_m , defined as

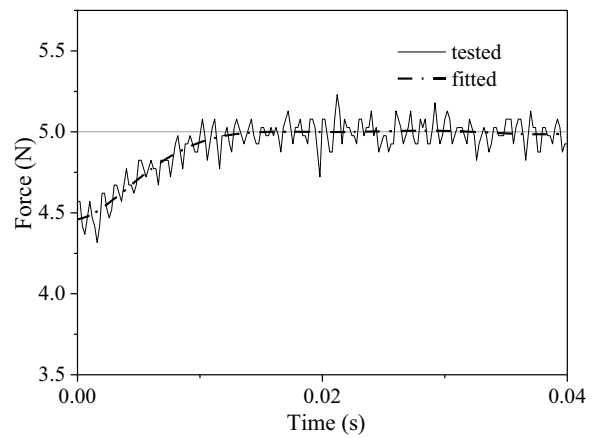


Figure 19 Test force of the explosive actuator

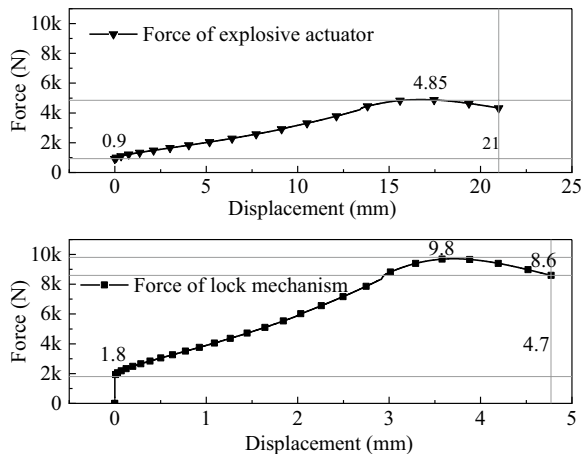


Figure 18 Output force of the explosive actuator and locking mechanism

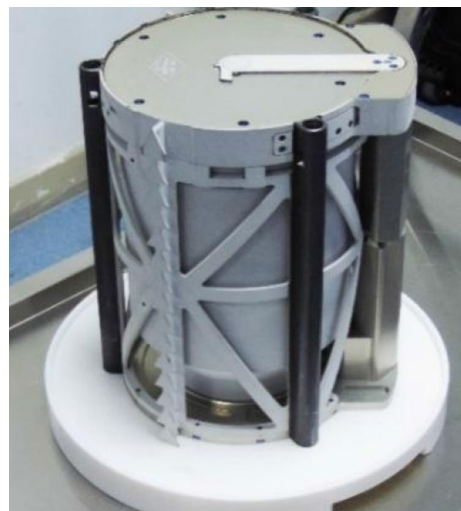


Figure 20 Encapsulation device of the Change-5

$\Phi_m = \arccos\left(\frac{(L_{BC} + y_W)^2 + L_{AC}^2 - L_{AB}^2}{2(L_{BC} + x)L_{AC}}\right)$, $0 < \Phi_m < \pi/2$. The parameters of the locking mechanism are listed in Table 8.

We performed a simulation of the locking mechanism. The forces outputted by the explosive actuator and locking mechanism are shown in Figure 18, which illustrates that the peak force of the explosive actuator was 4.8 kN, and its maximum displacement was 21 mm. The test results indicated that the explosive actuator could reach 5 kN, and the calculated results were similar to the actual values showed in Figure 19. The locking mechanism produced the highest thrust of 9.8 kN and a maximum displacement of 4.7 mm.

5 Results Discuss

We studied an encapsulation device of lunar samples as part of the third phase of the Chinese lunar exploration program. The research results were used in the Chang'e-5 explorer to complete a lunar SRM in 2020, which also proved the correctness and effectiveness of the research results. Figure 20 shows the encapsulation device of the Chang'e-5 explorer. The research results can be adapted to other sample return missions in the future.

The encapsulation device uses a combined rubber and metal seal. This design considers the environmental concerns and ease of manufacture. The rubber-ring seal has the advantages of simplicity, reliability, and good adaptability to the mechanical environment; however, it still has the property of low-temperature glass transition. The metal seal is better at withstanding extreme temperatures and performance than the rubber seal. However, metal seals are poorly adapted to the mechanical environment. Table 9 shows a comparison of the relevant characteristics. The temperature in deep-space can be as low as $-120\text{ }^\circ\text{C}$; thus, a hermetic seal made of rubber is at risk of failing. The combined assembly of rubber and metal can better accommodate the lunar environment.

The metal seal determines the hermetic leak rate of the combined seal, and an increase in the contact coefficient of the metal contact face can decrease the leak rate. The hermetic leak rate of the rubber seal approaches $10^{-7}\text{ Pa}\cdot\text{m}^3\cdot\text{s}^{-1}$, whereas that of the knife-edge seal tends to be $10^{-11}\text{ Pa}\cdot\text{m}^3\cdot\text{s}^{-1}$. The curve of the combined seal is the same as that of the metal seal, indicating that the

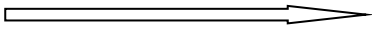

knife-edge seal is the primary seal of the encapsulation device. The knife-edge coated with Au improves the hermetic seal. The principle is that Au covers the machine traces on the sealing face, thereby increasing the contact coefficient of the sealing face. The test results indicated that the seal with the Au coating can be better than $5 \times 10^{-11}\text{ Pa}\cdot\text{m}^3\cdot\text{s}^{-1}$. We also found that the vibration degrades the seal performance seriously. The helium leak rate will increased significantly when the piece has finished the vibration test in advance. This result proves that the knife-edge seal is poorly adapted to the mechanical environment; thus a method for eliminating the impact of the vibration on the seal is a serious concern.

The sealing force is the design metric for the sealing assembly and is the key to creating the contact stress, contact width, and depth of the knife-edge, all of which affect the hermetic leak rate. It is obvious that the sealing process comprises three stages. In the first stage, the rubber-ring is squeezed into the sealing structure, and the sealing force increases with the displacement. The highest sealing force in the first stage is 118 N. Subsequently, the sealing force decreases, which implies that the sealing force after extruding the rubber-ring into the sealing structure is friction. In the second stage, the rubber-ring slid by 2 mm, and the sealing force was a sliding friction of 107 N. The third stage involves pressing the knife-edge into the Ag-In alloy, which still has the friction of the rubber. When the knife-edge is squeezed to a depth of 0.6 mm, the sealing force increases to 3890 N.

The OCM and locking mechanisms satisfied the requirements of the sealing unit. They also achieved the engineering goals of light weight, small volume, and low power. The OCM opens the cover by first lifting it and then rotating it, while closing it is achieved by doing the opposite. The OCM is a coaxial double-helical pair that outputs linear and rotational motions using only a rotational input. This novel principle is consistent with the opening and closing processes of the lid. The linear and rotational displacements of OCM were 41.5 mm and 120.2° , respectively. Its minimum input power was 0.3 W, and the weight of the OCM for the prototype was not greater than 200 g. The electric initiating explosive device aids in minimizing the mass of the locking mechanism. The orifice damping aids in minimizing the volume of the locking mechanism, increasing the output force, and eliminating impact, and its weight was not greater than 219 g. The output force of the explosive actuator was between 0.9 kN and 4.85 kN, and the maximum output displacement is 21 mm. The output force of the locking mechanism is between 1.8 kN and 9.8 kN with a buffer at the end of the output, and the maximum output displacement is 4.7 mm.

The indirect test results indicated that the locking mechanism must output more than 2.94 kN. With a

Table 9 Comparisons between the rubber and metal seal

Bad 		Good 
Performance	Rubber	Metal
Temperature environment	Rubber	Metal
Mechanical environment	Metal	Rubber
Reliability	Metal	Rubber

doubled safety margin, the locking mechanism outputs more than 7.8 kN. The safety factor of the sealing force is $S_a = 8.6/2.94 = 2.9$; therefore, $S_a > 2$, which met the design margin.

In summary, the sealing unit satisfied the sealing requirements, and the function of its mechanical unit was consistent with its sealing process. The coaxial double-helical drive and orifice damping solved the problems of a small volume and low power.

6 Conclusions

- (1) Aiming at the goal of the third phase of Chinese Lunar Exploration Programs, we investigated an encapsulation device for lunar samples. The final concept design of the encapsulation device satisfied the requirements of the explorer.
- (2) We built a theory of the hermetic seal, which revealed that the contact coefficient significantly affects the seal. An Au coating on the surface of the knife-edge improved the seal observably because of the increased contact coefficient. The coating process can also be used in other seals in vacuum. The coaxial double helical drive and orifice damping are the principal components of the mechanical units, and they make the encapsulation device work well and met the goals of lightweight, small volume, and low power. Finally, how to eliminate the impact of vibration on the seal is still an important research for the engineering prototype.

Acknowledgements

Not applicable.

Authors' Contributions

YD charged the whole trial and wrote the manuscript. CW and MJ finished the test. HL and YZ compile the soft and finished the simulation. XW assisted with the manuscript checking. All authors read and approved the final manuscript.

Funding

Supported by Research Foundation of CLEP of China (Grant No. TY3Q20110003).

Declarations

Competing Interests

The authors declare no competing financial interests.

Received: 8 September 2022 Revised: 6 May 2024 Accepted: 8 May 2024

Published online: 31 July 2024

References

- [1] C L Li, H Hu, M F Yang, et al. Characteristics of the lunar samples returned by the Chang'E-5 mission. *National Science Review*, 2022, 9(2): 1-13.
- [2] S Valencia, N Curran, J Flahaut. High priority returned lunar samples. *Bulletin of the AAS*, 2021, 53(4): 2023-2032.
- [3] R J Erickson. Lunar-16: An outstanding new achievement of Soviet space science foreign technology division. *Report of NASA*, 1970, Washington D.C., USA.
- [4] J H Allton. Lunar Sample: Apollo collection tools, curation handling, surveyorIII and soviet lunar samples. 2009, *Report of NASA*, Washington D.C., USA.
- [5] K Tsuno, E Okumura, Y Katsuyama, et al. Lidar on board asteroid explorer hayabusa. *International Conference on Space Optics*, Noordwijk, Netherlands, June 27-30, 2006: 1-7.
- [6] H Sawada, R Okazaki, S Tachibana, et al. Hayabusa2 sampler: Collection of asteroidal surface material. *Space Sci. Rev.*, 2017, 208(1-4): 81-106.
- [7] E Bierhaus, B Clark, J Harris, et al. The OSIRIS-REx spacecraft and the touch-and-go sample acquisition mechanism. *Space Sci. Rev.*, 2019, 214: 80-107.
- [8] X J Deng, Y H Zheng, S Y Jin, et al. Design and implementation of sampling, encapsulating, and sealing system of Chang'e-5. *Science China Technological Sciences*, 2021, 51(7): 753-762. (in Chinese)
- [9] Y G Du, X S Wang, C J Yan, et al. The parameter calculation of the metal seal structure for the lunar sample encapsulation. *Journal of Vacuum Science and Technology*, 2021, 41(5): 418-421. (in Chinese)
- [10] I Mikellides, P Shah, A Robinson, et al. Modelling and simulations of particle resuspension and transport for the assessment of terrestrial-borne biological contamination of the samples on the mars 2020 mission. *Planetary and Space Science*, 2020, 181: 104792.
- [11] B K Muirheada, A C Karpb, L Duvetc, et al. Mars sample return conceptual mission overview. *69th International Astronautical Congress (IAC)*, Bremen, Germany, October 1-5, 2018.
- [12] K A Farley, K H Williford, K M Stack, et al. Mars 2020 mission overview. *Space Sci. Rev.*, 2020, 216(142): 1-41.
- [13] J Grimes-York, J O'Brien. Sealing station mechanisms for the mars 2020 rover sample caching subsystem. *Process of the 45th Aerospace Mechanism Symposium*, May 13, 2020.
- [14] R Mihalache, D Mihai, G Megherelu, et al. Sealing technologies trade-off for a phobos sample return mission. *Transportation Research Procedia*, 2018, 29: 244-254.
- [15] Y Bar-Cohen, M Badescu, S Sherrit, et al. Synchronous separation, seaming, sealing and sterilization (s4) using brazing for sample containerization and planetary protection. *Sensors and Smart Structures Technologies for Civil, Mechanical, and Aerospace Systems*, Denver, Colorado, USA, March 12, 2018.
- [16] L Redmond, K Kriechbaum, P Younse, et al. Design of robust sealing mechanism for mars 2020 sample tubes. *Journal of Spacecraft and Rockets*, 2020, 57(5): 964-974.
- [17] R Gershman, Y Bar-Cohen, M Hendry, et al. Break-the-Chain technology for potential mars sample return. *2018 IEEE Aerospace Conference*, Big Sky, MT, USA, March 3-10, 2018: 1-21.
- [18] Laurence J Bement, Joseph T Sanok. Explosive joining for the mars sample return mission. *36th AIAA/ASME/SAE/ASEE Joint Propulsion Conference and Exhibit*, Las Vegas, Nevada, July 24-28, 2000.
- [19] P Younse, T de Alwis, P Backes, et al. Sample sealing approaches for mars sample return caching. *2012 IEEE Aerospace Conference*, March 3-10, 2012.
- [20] R C Moeller, L Jandura, K Rosette, et al. The sampling and caching subsystem (SCS) for the scientific exploration of jezero crater by the mars 2020 perseverance rover. *Space Sci. Rev.*, 2021, 217(5): 81-106.
- [21] E Kulczycki, C Galey, B Kennedy, et al. The development of a martian atmospheric sample collection canister. *IEEE Aerospace Conference Proceedings*, Big Sky, MT, USA, March 2-9, 2013: 1-10.
- [22] X J Wu, K C Wang, Z R Yang, et al. Study on preparation and characterization of In-Ag solders. *Precious Metals*, 2019, 40(1): 57-62.
- [23] J Chang, T X Cheng, Z Y Zhou, et al. Research on the performance of rubber seal structure at low temperature for manned spacecraft. *Journal of Vacuum Science and Technology*, 2021, 41(5): 435-447. (in Chinese)
- [24] A Roth. *Vacuum technology*. Beijing: China Machine Press, 1980. (in Chinese)
- [25] B Zhang, H C Hong, M Yu, et al. Leakage analysis and ground tests of knife edge indium seal to lunar sample return devices. *Proceedings*

of the Institution of Mechanical Engineers, Part G: *Journal of Aerospace Engineering*, 2019, 233(6): 2010–2022.

- [26] A Roth. The interface-contact vacuum sealing processes. *Journal of Vacuum Science & Technology*, 1972, 9(1): 14-23.
- [27] A Roth. The influence of the surface roughness on the specific leak rate of gasket seals. *Vacuum*, 1970, 20(10): 431-435.
- [28] J C Han, Y Li, P Gao, et al. Friction performance of space machine with MoS₂ solid lubrication coating in vacuum environment. *Journal of Mechanical Engineering*, 2017, 53(11): 61-67. (in Chinese)
- [29] M S Libório, G B Praxedes, L L F Lima, et al. Surface modification of M2 steel by combination of cathodic cage plasma deposition and magnetron sputtered MoS₂-TiN multilayer coatings. *Surface and Coatings Technology*, 2020, 284: 12-32.
- [30] H Singh, C Mutyala, L Doll. Rolling contact performance of a Ti-containing MoS₂ coating operating under ambient, vacuum, and oil-lubricated conditions. *Coatings*, 2019, 9(11): 1-12.
- [31] Z S Wang, W D He, F M Xu. *Principle and technique for gun propellant charge design*. Beijing: Beijing Institute of Technology Press, 2014. (in Chinese)
- [32] X B Zhang. *Interior ballistics of gun*. Beijing: Beijing Institute of Technology Press, 2014. (in Chinese)

Yonggang Du born in 1975, is currently a senior engineer at *Lanzhou Institute of Physics, China Academy of Space Technology, China*. His research interests include mechanism and control, mechanism in space, extraterrestrial object sampling technology.

Chunyong Wang born in 1982, is currently a senior engineer at *Lanzhou Institute of Physics, China Academy of Space Technology, China*. His research interests include extraterrestrial object sampling technology.

Haoling Li born in 1984, is currently a senior engineer at *Lanzhou Institute of Physics, China Academy of Space Technology, China*.

Ying Zhou born in 1979, is currently a senior engineer at *Lanzhou Institute of Physics, China Academy of Space Technology, China*.

Ming Ji born in 1980, is currently an engineer at *Lanzhou Institute of Physics, China Academy of Space Technology, China*.

Xuesong Wang born in 1975, is currently a professor in engineering at *Lanzhou Institute of Physics, China Academy of Space Technology, China*.